

Article

Nonlinear Slippage of Tensile Armor Layers of Unbonded Flexible Riser Subjected to Irregular Loads

Qingsheng Liu ^{1,†} , Zhongyuan Qu ^{1,†}, Xiaoya Liu ¹, Jiawei He ², Gang Wang ¹, Sicong Wang ^{1,*} and Feng Chen ^{1,*}

¹ School of Mechanical and Electric Engineering, Soochow University, Suzhou 215131, China

² Naval Research Institute (NVRT), Beijing 100161, China; hjw_sjtu@163.com

* Correspondence: scwang8901@suda.edu.cn (S.W.); chenfeng508@suda.edu.cn (F.C.);

Tel.: +86-512-65790196 (S.W. & F.C.)

† These authors contributed equally to this work.

Abstract: The unbonded flexible riser has been increasingly applied in the ocean engineering industry to transport oil and gas resources from the seabed to offshore platforms. The slippage of helical layers, especially the tensile armor layers of unbonded flexible risers, contribute to the nonlinear hysteresis phenomenon, which is a research hotspot and difficulty. In this paper, on the basis of a typical eight-layer unbonded flexible riser model, the nonlinear slippage of a tensile armor layer and the corresponding nonlinear behavior of an unbonded flexible riser subjected to irregular external loads are studied by numerical modeling with detailed cross-sectional properties of the helical layers, and are verified through a theoretical method considering the coupled effect of the external loads on the unbonded flexible riser. Firstly, the balance equation of each layer considering the effect of external loads is established based on functional principles, and the overall theoretical model of the unbonded flexible riser is set up in consideration of the contact between adjacent layers. Secondly, the numerical modeling of each separate layer within the unbonded flexible riser, including the actual geometry of the carcass and pressure armor layer, is established, and solid elements are applied to all the interlayers, thus simulating the nonlinear contact and friction between and within interlayers. Finally, after verification through test data, the behavior of the unbonded flexible riser under the cyclic axial force, torsion, bending moment, and irregular external and internal pressure is studied. The results show that the tensile armor layer can slip under irregular loads. Additionally, some suggestions related to the analysis of unbonded flexible risers under irregular loads are drawn in the end.

Keywords: unbonded flexible riser; tensile armor layer; slippage; irregular loads; numerical method; theoretical method



Citation: Liu, Q.; Qu, Z.; Liu, X.; He, J.; Wang, G.; Wang, S.; Chen, F. Nonlinear Slippage of Tensile Armor Layers of Unbonded Flexible Riser Subjected to Irregular Loads. *J. Mar. Sci. Eng.* **2024**, *12*, 818. <https://doi.org/10.3390/jmse12050818>

Academic Editor: José António Correia

Received: 6 April 2024
Revised: 11 May 2024
Accepted: 12 May 2024
Published: 14 May 2024



Copyright: © 2024 by the authors. Licensee MDPI, Basel, Switzerland. This article is an open access article distributed under the terms and conditions of the Creative Commons Attribution (CC BY) license (<https://creativecommons.org/licenses/by/4.0/>).

1. Introduction

An unbonded flexible riser (see Figure 1) is made of multiple separate layers with different geometric and mechanical properties, and is a key equipment to transport gas and oil resources from the seabed to offshore platforms. Recently, unbonded flexible risers have gained a wider application for their advantages of light weight, resistance to large bending deformation and corrosion, and recyclability, and have become a unique equipment for the offshore oil and gas industry in deep waters. The unbonded flexible riser has become a necessary pipeline in the development of offshore oil and gas resources of the deep sea and has important engineering applications and strategic value for the development of deep-sea resources.

The development of marine oil and gas resources from shallow waters to deep waters is the trend of the world's marine oil and gas resource development. The fixed platform production system is typically used in the process of developing deep-sea oil and gas resources. This system is limited by the water depth, and usually adopts the combination of a floating production system and an underwater production system, which requires the

use of a large number of pipelines, such as dynamic risers, spanning pipelines, submarine static pipelines, etc. The harsh working environment of the sea conditions puts severe requirements on the structural performance of steel pipelines. The application of steel pipelines in the deep sea is limited due to fatigue caused by ocean current fluctuations, poor corrosion resistance, difficulties in laying the pipelines during construction, and long periods of construction. The unbonded flexible riser has a special structure in that each of the interlayers is relatively independent and can be moved relative to each other. This gives it better flexibility and adaptability than steel pipes, and it has thus become a necessary pipeline for ocean development, especially for deep-sea development.

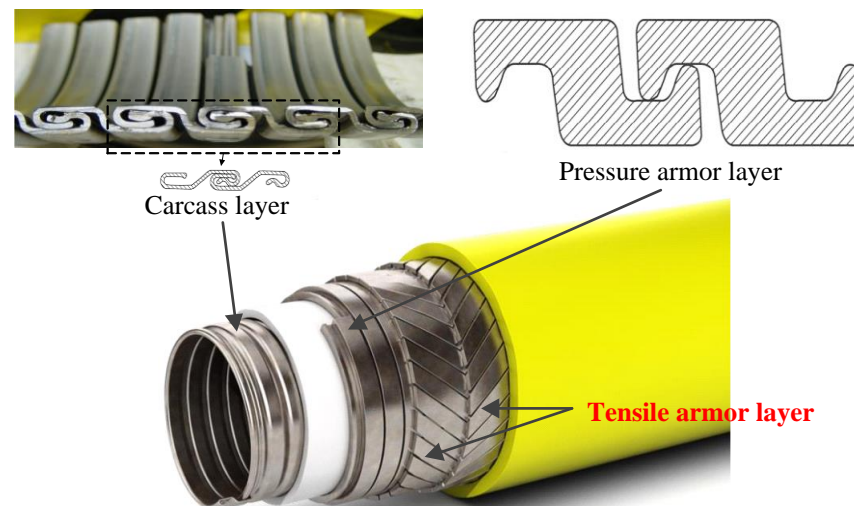


Figure 1. Typical unbonded flexible riser and sketch of carcass and pressure armor layer.

The analytical methods for assessing the cross-sectional mechanical properties of unbonded flexible risers typically include two categories, theoretical analysis and numerical simulation, since the cost of unbonded flexible riser specimens is high and the test conditions are harsh. The method of analyzing the mechanical properties of flexible riser sections can be divided into two stages: axisymmetric analysis (behavior under axial force, torsion, and internal and external pressure) and bending analysis. The interlayer contact pressure required for the bending response analysis needs to be obtained from the axisymmetric response analysis. A large number of experimental tests show that the axisymmetric response of the flexible riser is basically linear, while the bending response shows obvious hysteresis behavior.

For theoretical methods under axisymmetric loads, early studies generally only focused on the overall response of the riser under a certain load alone, and the response of each interlayer could not be decoupled [1]; subsequent studies established the equilibrium equations of each interlayer, and gradually considered the thickness deformation of different layers and established the geometrical relationship between layers, so as to establish the overall stiffness matrix of the unbonded flexible riser [2–5]. The understanding about the slippage of helical layers in unbonded flexible risers has gone through a process from simple to complex, and the core idea is to consider the helical tendon from the non-slip phase to the full slip phase, which gradually considers the bending moment–curvature relationship in the partial slip phase to improve the understanding of the slippage of the helical tendon [6–10]. Féret and Bournazel [11] were among the early investigators of the structural response of the unbonded flexible riser; they presented an analytical method to quickly assess the stress of the helical tendon, while ignoring the effects of internal and external pressures and interlayer gaps in the unbonded flexible riser model, and it was concluded that the non-metallic cylindrical shell layer only transmits the interlayer pressures and ignores the role of its axial stiffness. Keadze et al. [12,13] made a great contribution to the theoretical modeling of unbonded flexible risers: for axisymmetric anal-

ysis, they established the balance equation of each layer and took the relationship between adjacent layers into account; for bending analysis, they divided the bending process into three stages, no slip, partial slip, and full slip, and gave the corresponding bending stiffness expression. Then, Dong et al. [14], based on Kebabze's theoretical model, accurately calculated the curvature and deflection changes of the helical tendon and regained the bending stiffness induced by the effects of local bending and torsion of the helical tendon, and at the same time recalculated the partially slipping bending stiffness with an explicit expression, which greatly simplified the calculation process. Karathanasopoulos et al. [15] presented an analytical model to characterize the mechanical response of helical constructions, such as cables and ropes, to thermal loads, providing closed-form expressions to compute the forces and moments induced by homogeneous and non-homogeneous temperature fields. Kee-Jeung Hong et al. [16] developed a mesoscale mechanical model that captures the bending behavior of helically wrapped cables subjected to tension, taking into account the cable's nonlinear dissipative characteristics due to wire slippage under the influence of frictional forces. Current research mainly focuses on how to accurately describe the slip characteristics of the helical tendon, including the tensile armor layer bending hysteresis model established by considering different friction models and based on the theory of bending beams [17,18]; the analytical analysis model considering the deformation characteristics of the tensile armor layer under the action of riser torque and bending around the axis [19]; the bending hysteresis model established by considering the effect of shear deformation of the cylindrical shell layer structure in the riser [20]; and so on.

Numerical methods have evolved from equivalent simplified models to models that account for detailed geometric properties. Numerical methods need to simulate, as much as possible, the action of the layers of an unbonded flexible riser as well as the mutual contact between the layers, and most of the early numerical models of unbonded flexible risers simplified the internal complex structure to some extent [21,22]. Bahtui et al. [23,24] established the separate layer model and took into account the nonlinear contact within the unbonded flexible riser, which could provide the ability to simulate the bending behavior of unbonded flexible riser; however, they did not account for the detailed cross-sectional properties of the carcass layer and the pressure armor layer. Leroy and Perdrizet et al. [25,26] discussed the explicit and implicit solution algorithms, and their results showed that the explicit algorithm needs to take into account the influence of inertial effects on the results of the calculations, and accordingly the computation time is long. On the contrary, the standard solving algorithm has a higher solving efficiency; however, the calculation is not easy to converge while considering the geometric and material nonlinearities as well as the nonlinearities of interlayer and intralayer mutual contact. With the improvement of computer computational performance, more and more scholars began to consider the establishment of numerical models containing the detailed geometric characteristics of unbonded flexible risers [20,27–34]. Among them, Ren et al. [35–37] numerically simulated the unbonded flexible riser model using its actual geometry, including the S-type carcass layer and the Z-type pressure armor layer. The complex behavior of unbonded flexible risers under coupling loads can further be simulated using their model. Liu et al. [38,39] extended the steel homogeneous tensile armor layer model to one that can simultaneously account for the steel and composite tensile armor layers and carried out the calculation of the mechanical properties of the composite tensile armor layer in different working conditions by establishing a numerical model with detailed geometric properties. The accuracy of the theoretical and numerical methods was mutually verified.

This study introduces a comprehensive experiment to understand the nonlinear slip-page behavior of tensile armor layers in unbonded flexible risers under irregular loads by numerical and theoretical methods. A significant advancement over existing research by integrating detailed cross-sectional properties into both theoretical and numerical models is present. The novelty lies in its ability to capture the complex interactions between layers, accounting for the coupled effects of external loads and interlayer contact. The main achievements include the development of an eight-layer unbonded flexible riser model that

simulates real-world conditions with high fidelity, and the validation of the model against test data. The results of this study provide new insights into the hysteresis phenomenon associated with the slippage of tensile armor layers, offering practical implications for the design and operation of deep-sea oil and gas infrastructure. By focusing on the nonlinear behavior under irregular loads, this research contributes to the ongoing efforts to enhance the reliability and safety of unbonded flexible risers in the offshore industry.

2. Theoretical Formulations

A simple sketch of the deformation of an unbonded flexible riser can subject to external loading is presented in Figure 2. The following assumptions have to first be introduced:

1. The external loads of axisymmetric loads and the bending moment can be decoupled.
2. All layers in the model are assumed to be in the small deformation stage and neglect the material nonlinearity for the cross-sectional analysis.
3. The riser has sufficient length ($L/D \cong 10$, where L is the initial length of riser and D is the outer diameter of riser).
4. The riser segment is assumed to be far away from the bending stiffener and the initial imperfection of the riser is also neglected, and it is assumed that each layer of the riser has the same axial elongation and torsion angle along the central axis.
5. For helical layers, the frictional energy due to the slippage of helical tendon is neglected.
6. The anti-friction layer is simplified as a cylindrical layer.
7. The thickness deformations of the carcass layer as well as the pressure armor layer are neglected.
8. When studying the fracture of the tensile armor layer, the tensile armor layer is considered to have lost its bearing capacity when it reaches the yield stress.
9. The static and dynamic coefficients of friction between the layers are equal.
10. When applying the bending moment, the axial direction of the tendon is the only slip direction.
11. The only contribution to the critical bending curvature is the initial axisymmetric load and the interlayer pressure caused by the bending moment is ignored.

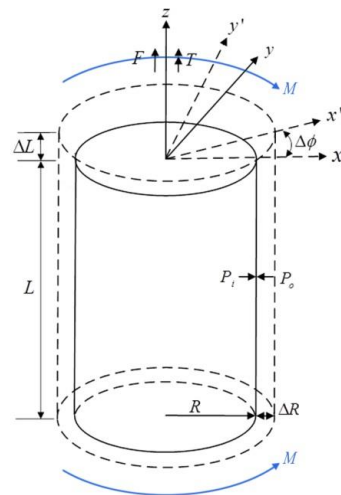


Figure 2. Deformation of unbonded flexible riser after external loading.

2.1. Analytical Modeling of Cylindrical Layer by Axisymmetric Loads

It can be seen in Figure 2 that the axisymmetric loads include axial force F , torsion T , internal and external pressures P_i and P_o . The energy applied by axisymmetric loads can be assumed to be given by [12,36]:

$$W = F\Delta L + T\Delta\phi + P_i\Delta V_i - P_o\Delta V_o \quad (1)$$

where ΔL is the axial deformation, $\Delta\varphi$ is the rotational angle about the axial direction, and ΔV_i and ΔV_o are the internal and external volumetric distortions, separately, and can be given as

$$\Delta V_i = \pi \left(R_i + \Delta R - \frac{\Delta t}{2} \right)^2 (L + \Delta L) - \pi R_i^2 L \approx \pi R_i L (2R_m \varepsilon_2 - t\varepsilon_3 + R_i \varepsilon_1) \quad (2)$$

$$\Delta V_o = \pi \left(R_o + \Delta R + \frac{\Delta t}{2} \right)^2 (L + \Delta L) - \pi R_o^2 L \approx \pi R_o L (2R_m \varepsilon_2 + t\varepsilon_3 + R_o \varepsilon_1) \quad (3)$$

where R_i and R_o are the internal and external radii of the cylindrical layers, separately; R_m is the average radius; L is the initial length of the layer; t and Δt are the thickness and thickness deformation of the cylindrical layer; and the strains of the cylindrical layer are defined by $\varepsilon_1 = \Delta L/L$, $\varepsilon_2 = \Delta R/R_m$, and $\varepsilon_3 = \Delta t/t$. Thus, Equation (1) can be rewritten as:

$$W = (F\varepsilon_1 + T\gamma)L + \pi P_i R_i L (2R_m \varepsilon_2 - t\varepsilon_3 + R_i \varepsilon_1) - \pi P_o R_o L (2R_m \varepsilon_2 + t\varepsilon_3 + R_o \varepsilon_1) \quad (4)$$

where $\gamma = \Delta\varphi/L$.

According to the above strains, the derivation of the work done by the external axisymmetric loads can be obtained [40]. For anisotropic materials, the relationship between strain and stress can be given based on Hooke's law. The strain energy U can be presented as:

$$\begin{aligned} U &= \frac{1}{2} \int_V (\sigma_1 \varepsilon_1 + \sigma_2 \varepsilon_2 + \sigma_3 \varepsilon_3 + \tau_{12} \gamma_{12}) dV \\ &= \frac{1}{2} \int_V [(\lambda + 2G)(\varepsilon_1^2 + \varepsilon_2^2 + \varepsilon_3^2) + 2\lambda(\varepsilon_1 \varepsilon_2 + \varepsilon_1 \varepsilon_3 + \varepsilon_2 \varepsilon_3) + GR_m^2 \gamma^2] dV \end{aligned} \quad (5)$$

where $\sigma_1, \sigma_2, \sigma_3$, and τ are the corresponding stresses of each direction; E is the Young's modulus and μ is the Poisson's ratio; $G = \frac{E}{2(1+\mu)}$ is the shear modulus; and parameter $\lambda = \frac{\mu E}{(1+\mu)(1-2\mu)}$.

Substituting the volume of the cylindrical layer $V = \pi(R_o^2 - R_i^2)L$ and applying the partial derivatives for each strain yields:

$$\begin{aligned} \frac{\partial U}{\partial \varepsilon_1} &= [(\lambda + 2G)\varepsilon_1 + \lambda(\varepsilon_2 + \varepsilon_3)]AL \\ \frac{\partial U}{\partial \gamma} &= \pi GR_m^2 \gamma (R_o^2 - R_i^2)L \approx \pi G \gamma (R_o^4 - R_i^4)L \\ \frac{\partial U}{\partial \varepsilon_2} &= [(\lambda + 2G)\varepsilon_2 + \lambda(\varepsilon_1 + \varepsilon_3)]AL \\ \frac{\partial U}{\partial \varepsilon_3} &= [(\lambda + 2G)\varepsilon_3 + \lambda(\varepsilon_1 + \varepsilon_2)]AL \end{aligned} \quad (6)$$

where $A = \pi(R_o^2 - R_i^2)$.

Based on the functional principle, the relationship between the total potential energy and the work done by the external loads and internal energy can be given by:

$$\partial \Pi = \partial W - \partial U = 0 \quad (7)$$

The equilibrium equation for the cylindrical layer can be obtained by combining Equations (5)–(7) [35,38]:

$$\begin{bmatrix} k_{11} & k_{12} & k_{13} & k_{14} \\ k_{21} & k_{22} & k_{23} & k_{24} \\ k_{31} & k_{32} & k_{33} & k_{34} \\ k_{41} & k_{42} & k_{43} & k_{44} \end{bmatrix} \begin{bmatrix} \Delta L/L \\ \Delta\varphi/L \\ \Delta R/R_m \\ \Delta t/t \end{bmatrix} = \begin{bmatrix} F + \pi P_i R_i^2 - \pi P_o R_o^2 \\ T \\ 2\pi R_m (P_i R_i - P_o R_o) \\ -\pi t (P_i R_i + P_o R_o) \end{bmatrix} \quad (8)$$

where

$$\begin{aligned}
 k_{11} &= \frac{\mu EA}{(1+\mu)(1-2\mu)} + \frac{EA}{1+\mu} & k_{13} &= k_{31} = \frac{\mu EA}{(1+\mu)(1-2\mu)} \\
 k_{22} &= \frac{E}{2(1+\mu)} \cdot \frac{\pi}{2} (R_o^4 - R_i^4) & k_{24} &= k_{42} = 0 \\
 k_{34} &= k_{43} = \frac{\mu EA}{(1+\mu)(1-2\mu)} & k_{12} &= k_{21} = 0 \\
 k_{14} &= k_{41} = \frac{\mu EA}{(1+\mu)(1-2\mu)} & k_{23} &= k_{32} = 0 \\
 k_{33} &= \frac{\mu EA}{(1+\mu)(1-2\mu)} + \frac{EA}{1+\mu} & k_{44} &= \frac{\mu EA}{(1+\mu)(1-2\mu)} + \frac{EA}{1+\mu}
 \end{aligned}$$

2.2. Analytical Modeling of Helical Layer by Axisymmetric Loads

For the carcass layer and pressure armor layer with complex cross-sections, only the axial deformation is considered, while for the tensile armor layer with a regular cross-section, the radial deformation is also involved, and the sketch of a loaded helical tendon is presented in Figure 3. Based on the geometric properties of the helical tendon and assuming the laying angle is α , the axial strain ϵ_a and the radial strain ϵ_r can be defined by [11,12,36]:

$$\begin{aligned}
 \epsilon_a &= \cos^2 \alpha \frac{\Delta L}{L} + R_m \sin \alpha \cos \alpha \frac{\Delta \phi}{L} + \sin^2 \alpha \frac{\Delta R}{R_m} \\
 \epsilon_r &= \frac{\Delta t}{t}
 \end{aligned} \tag{9}$$

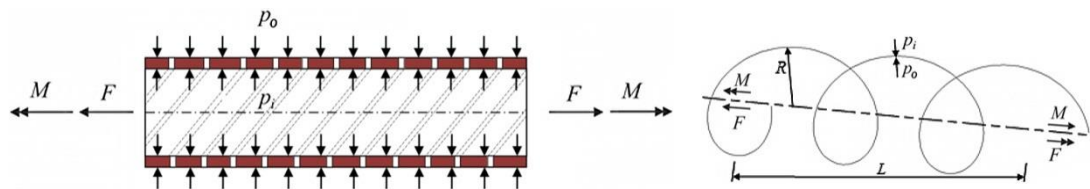


Figure 3. Force schematic diagram of the helical layer.

The strain energy of a single helical tendon is calculated by [12,38]:

$$U_s = \frac{n}{2} \int_V (\sigma_a \epsilon_a + \sigma_r \epsilon_r) dV \tag{10}$$

where n is the number of helical tendons and σ_a and σ_r are the corresponding stresses of the helical tendon.

Similar to the deduction process in Section 2.1, the final equilibrium equation for the helical layer can be presented as follows [12,38,39]:

$$\begin{bmatrix} k_{11} & k_{12} & k_{13} & k_{14} \\ k_{21} & k_{22} & k_{23} & k_{24} \\ k_{31} & k_{32} & k_{33} & k_{34} \\ k_{41} & k_{42} & k_{43} & k_{44} \end{bmatrix} \begin{bmatrix} \Delta L/L \\ \Delta \phi/L \\ \Delta R/R_m \\ \Delta t/t \end{bmatrix} = \begin{bmatrix} F + \pi P_i R_i^2 - \pi P_o R_o^2 \\ T \\ 2\pi R_m (P_i R_i - P_o R_o) \\ -\pi t (P_i R_i + P_o R_o) \end{bmatrix} \tag{11}$$

where

$$\begin{aligned}
 k_{11} &= \frac{nEA}{1-\mu^2} \cos^3 \alpha & k_{12} &= \frac{nEAR_m}{1-\mu^2} \sin \alpha \cos^2 \alpha \\
 k_{13} &= k_{31} = \frac{nEA}{1-\mu^2} \sin^2 \alpha \cos \alpha & k_{14} &= k_{41} = \frac{nEA\nu}{1-\mu^2} \cos \alpha \\
 k_{22} &= \frac{nEAR_m^2}{1-\mu^2} \sin^2 \alpha \cos \alpha & k_{23} &= k_{32} = \frac{nEAR_m}{1-\mu^2} \sin^3 \alpha \\
 k_{24} &= k_{42} = \frac{nEAR_m \mu}{1-\mu^2} \sin \alpha & k_{33} &= \frac{nEA \sin^4 \alpha}{1-\mu^2 \cos \alpha} \\
 k_{34} &= k_{43} = \frac{nEA \mu \sin^2 \alpha}{1-\mu^2 \cos \alpha} & k_{44} &= \frac{nEA}{(1-\mu^2) \cos \alpha}
 \end{aligned}$$

By combining the equilibrium equations of each layer, the force–strain relationship can be established. In addition to solving the unknowns, the geometrical relationships between

adjacent layers should be considered. Based on the restriction of geometric continuity, the interlayer contact relationship between adjacent layers is given by the following equation:

$$R_m^j + \Delta R^j + \frac{t^j + \Delta t^j}{2} = R_m^{j+1} + \Delta R^{j+1} - \frac{t^{j+1} + \Delta t^{j+1}}{2} \tag{12}$$

where j stands for the number of a separate interlayer.

When the neighboring layer starts to separate, i.e., there is gap between neighboring layers, the contact pressure is set as 0.

Based on the above equation, the analytical solution under axisymmetric loads can be obtained.

2.3. Analytical Modeling of Unbonded Flexible Riser by Bending Moment

For a homogeneous isotropic cylindrical shell layer, the bending characteristics can be obtained according to the flat section assumption [39]:

$$M = EI\kappa \tag{13}$$

where EI is the bending stiffness; M stands for the bending moment; and κ is the corresponding curvature.

The bending stiffness of a helical layer can be divided into three stages according to the slip phase. When in the phase where the helical tendon is bonded to the adjacent layer, based on Equation (9), the strain of the helical tendon, in consideration of the geometric angle of helical tendon (see Figure 4) and plane assumption under bending moment, is simplified by only considering the axial strain [12–14]:

$$\varepsilon_a = R_m \cos^2 \alpha \sin \theta \kappa \tag{14}$$

where $\theta = \theta_{j1} + \theta_{j2} = \frac{2\pi j}{n} + z \frac{\tan \alpha}{R_m}$; z is the distance in the axial direction of the unbonded flexible riser.

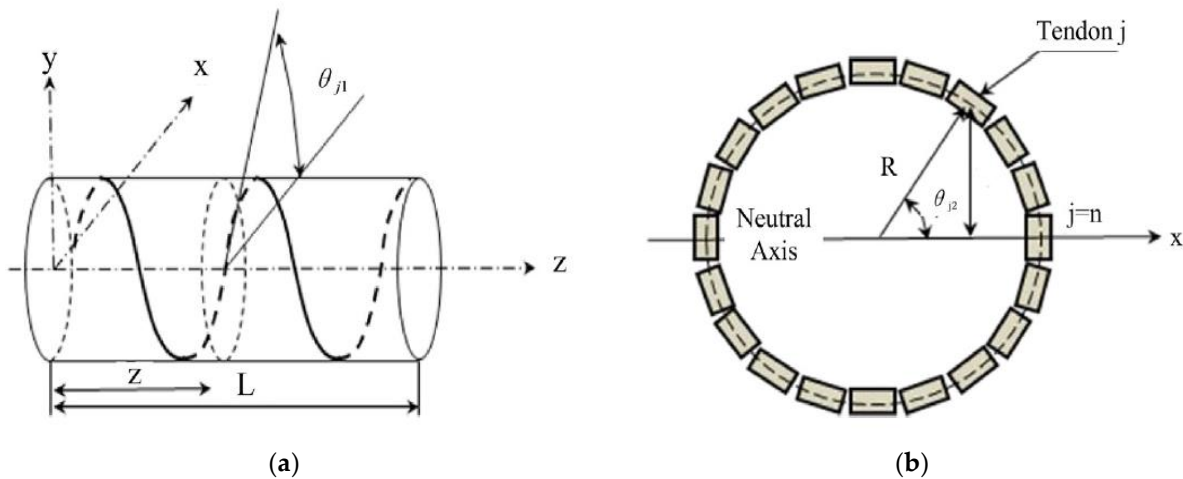


Figure 4. Sketch of geometric helical tendon; (a) Geometric angle of a helical tendon; (b) Cross-section angle of the helical tendon.

According to the functional principle, the following relationship of the tensile armor layer during the non-slip stage can be obtained [12,14]:

$$\begin{aligned} M &= nEAR_m^2 \cos^3 \alpha \cdot \kappa / 2 \\ EI_{ns} &= nEAR_m^2 \cos^3 \alpha / 2 \end{aligned} \tag{15}$$

Based on the above assumptions, the critical curvature κ_{cr} is calculated by the contact pressure of axisymmetric loads [12,39]:

$$\kappa_{cr} = \frac{P_i \mu_i + P_o \mu_o}{Et \sin \alpha \cos^2 \alpha \cos \theta} \tag{16}$$

where μ_i and μ_o are the friction coefficients between contact layers and P_i and P_o are the corresponding contact pressures from the axisymmetric analysis.

When $\kappa_{cr}^{min} < \kappa < \pi \cdot \kappa_{cr}^{min} / 2$, the tensile armor layer is in the partial slip stage, and the bending characteristics are presented as [14]:

$$\begin{aligned} M &= 4EI_{ns}\kappa_{cr}^{min}(\sin \theta_{cr} - \theta_{cr} \cos \theta_{cr}) / \pi + EI_{ns}\kappa[\pi - 2\theta_{cr} + \sin 2\theta_{cr}] / \pi \\ EI_{ps} &= EI_{ns} - EI_{ns}(2\theta_{cr} - \sin 2\theta_{cr}) / \pi - \frac{4\xi \sin \theta_{cr} EI_{ns}}{\tan(\theta_{cr} / \xi) \pi} \left(\theta_{cr} \cos \frac{\theta_{cr}}{\xi} - \sin \theta_{cr} \right) \end{aligned} \tag{17}$$

When the bending curvature exceeds $\pi \cdot \kappa_{cr}^{min} / 2$, the tensile armor layer enters the full slip phase and loses its corresponding bending stiffness, which can be set to zero. The remaining bending stiffness is caused by the deformation of the helical tendon [14]:

$$\begin{aligned} M_{bt} &= \frac{n\kappa}{2} [EI_n(1 + \sin^2 \alpha) \cos \alpha + EI_b \cos^7 \alpha + GJ \sin^2 \alpha \cos^5 \alpha] \\ EI_{bt} &= \frac{n}{2} [EI_n(1 + \sin^2 \alpha) \cos \alpha + EI_b \cos^7 \alpha + GJ \sin^2 \alpha \cos^5 \alpha] \end{aligned} \tag{18}$$

where I_n stands for the inertia moment of the helical tendon; I_b is the bi-normal inertia moment; and J is the torsional inertia moment of helical tendon.

The effect of axisymmetric loads is also considered in this paper and is given by the following equation [39]:

$$M_p^h = \frac{nbR_oP_o - nbR_iP_i}{2\kappa^2 \cos \alpha} \left(2 \sin \frac{L\kappa}{2} - \frac{\sin L\kappa}{2} - \sin \frac{L\kappa}{2} \cos \frac{L\kappa}{2} \right) \tag{19}$$

Additionally, for the irregular external pressure applied to the outer sheath, an integral approach is used to synthesize the effect of the external pressure.

3. Numerical Simulation

Detailed geometric and material properties of unbonded flexible riser models are very rare since the riser model is not only difficult to produce, but also very expensive, and there are few published riser models with detailed properties. In 1996, Witz [41] presented some classic experiments of a typical 2.5-inch unbonded flexible riser model with eight layers, which not only includes detailed geometric properties, but also detailed experimental measurements and boundary conditions, and many scholars have conducted research based on these tests since then. Thus, Witz’s model is also used to simulate the complex behavior of unbonded flexible risers in this paper. The corresponding geometric and material characteristics are presented in Table 1. Additionally, a sketch of the numerical model, including the all-inclusive helical layer with detailed geometric properties, is illustrated in Figure 5.

Some settings have to be established first. At first, the numerical model should have sufficient length, typically no less than twice the tensile armor pitches [42], to avoid the effect of the stress concentration phenomenon at the end of riser model. To accurately capture the behavior of the unbonded flexible riser, a 1.0-m numerical model was constructed using the finite element (FE) software Abaqus of 6.13 version. This model’s length is more than twice the pitch of the tensile armor layer to ensure accurate representation (as detailed in Table 1). The FE model utilized 8-node linear elements with incompatible modes to simulate the solid layers and account for geometric nonlinearities. Then, since there are a large number of geometric and contact nonlinearities within the numerical model, the explicit solution method is adopted for calculations. The simulations were conducted on a high-performance computing cluster, requiring approximately 20 h of processing time on

64 cores. Also, two reference points (see Figure 5, RP1 and RP2) are set at the geometric center of both cross-sections of the unbonded flexible riser model and all the boundary nodes of each separate interlayer are bounded onto the reference points, thus applying the boundary conditions and external loads. Additionally, a general contact is applied within the numerical model, and the tangential behavior is simulated by using the Coulomb friction model [27], where the corresponding frictional coefficient is 0.1 [43]. The inertia effect must be taken into account for the explicit solution method and the kinetic energy during the calculation process should be controlled. As a consequence of controlling the kinetic energy, which is under 5% compared with the internal energy, during simulation, a smooth step loading method is applied to extend the simulation time and decrease the inertia effect. Two steps are applied for the analysis of the bending behavior: an initial external pressure is applied first to simulate the prestressing state and then the bending moment is applied.

Table 1. Geometric and material properties of unbonded flexible riser model.

Layer Number	Layer Type	Section Size (mm ²)	Number of Tendons	Inner Radius (mm)	Outer Radius (mm)	Laying Angle (°)	Material	Young's Modulus (GPa)	Poisson's Ratio
1	Carcass	19.60	1	31.60	35.10	−87.5	AISI 304	205	0.29
2	Pressure sheath	-	-	35.10	40.00	-	Nylon 12	0.28	0.30
3	Zeta layer	5.55	1	40.05	46.25	−85.5	FI-15	205	0.29
4	Anti-friction layer	-	-	46.25	47.75	-	Nylon 11	0.30	0.30
5	Inner tensile armor layer	18.00	40	47.75	50.75	−35.0	FI-41	205	0.29
6	Anti-friction layer	-	-	50.75	52.25	-	Nylon 11	0.30	0.30
7	Outer tensile armor layer	18.00	44	52.25	55.25	35.0	FI-41	205	0.29
8	Fabric tape	4.50	-	55.25	55.75	-	-	0.60	0.30

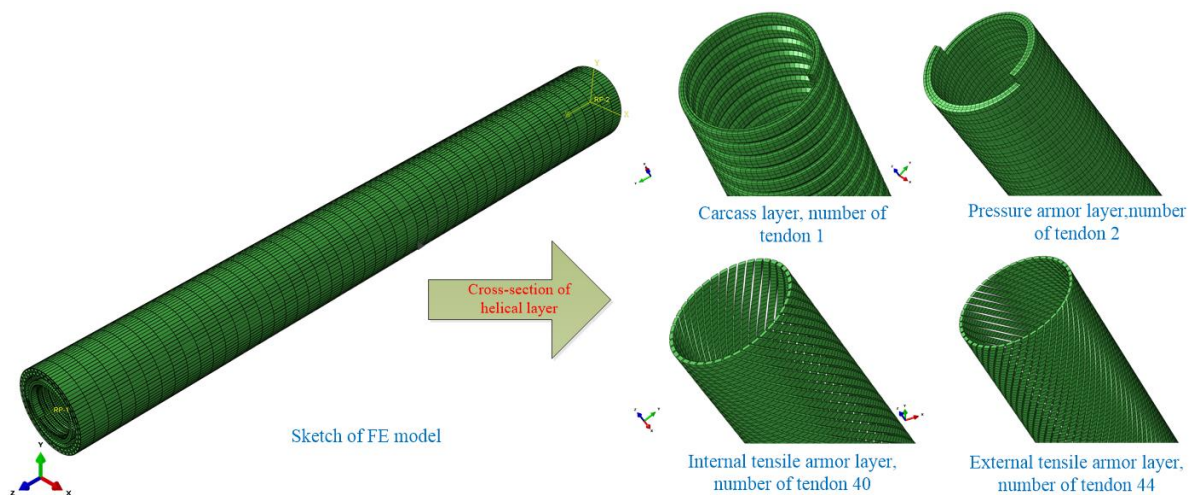


Figure 5. Sketch of finite element model of unbonded flexible riser.

4. Model Verification

4.1. Axial Tensile Behavior of Unbonded Flexible Riser

The axial tensile behavior is presented in this section to verify the proposed theoretical and numerical methods based on Witz’s test [41]. A total axial tension of 500 kN is applied to RP1 and the corresponding boundary condition is top-end free, while the other reference point, RP2, is set as fixed of all degrees of freedom. A quasi-static method is used to apply the axial tension, and in order to minimize the inertia effect, the tension loading duration is increased while ensuring computational efficiency. The axial tension–elongation curves of the unbonded flexible riser model by different methods are shown in Figure 6, and the axial tensile stiffness can be found in Table 2. During the numerical simulation, the ratio

of kinetic energy to internal energy is presented in Figure 7, where the ratio is no more than 5%.

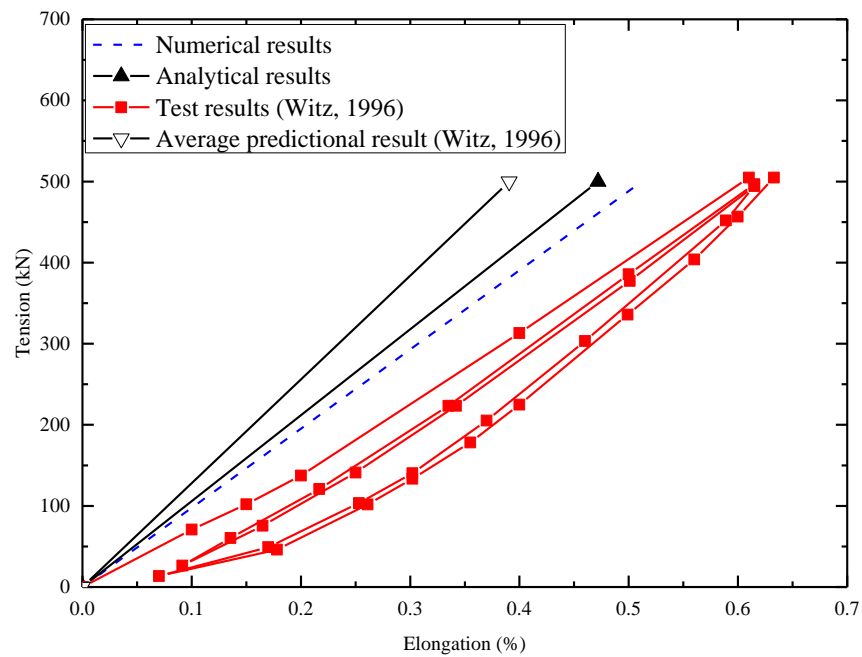


Figure 6. Axial tension–elongation curves of different methods [41].

Table 2. Axial stiffness by different methods.

Method	Axial Tensile Stiffness (MN)	Axial Compressive Stiffness (MN)
Analytical method	105.88	1.46
Numerical method	99.19	1.49
Experimental method	91.19	-

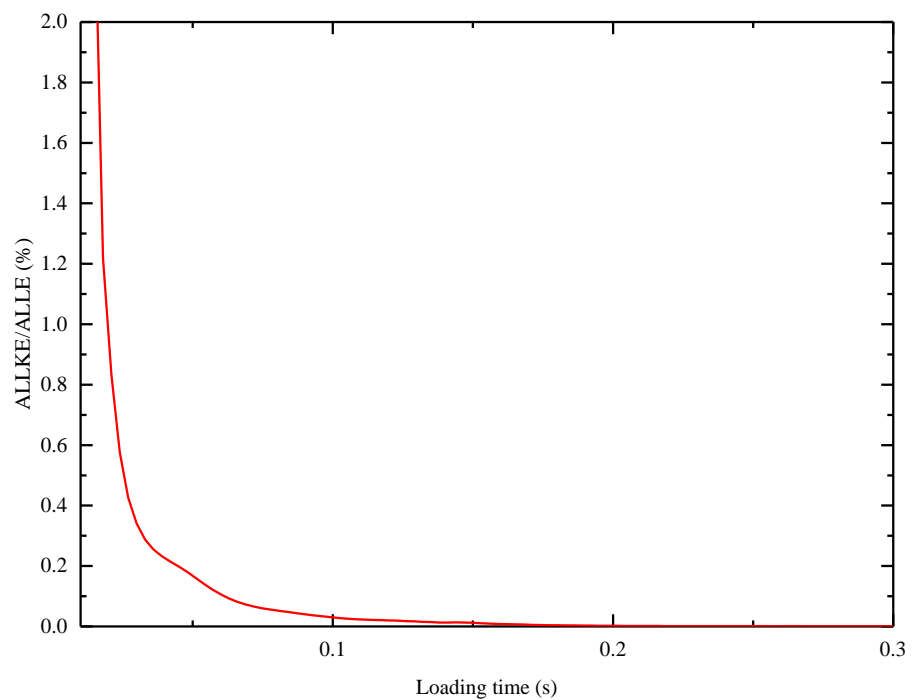


Figure 7. Ratio of kinetic energy to internal energy.

Unlike the test results, from Figure 6, the numerical and theoretical results do not exhibit significant nonlinearities since the tensile armor layers do not have obvious slippage. However, in terms of the axial tensile stiffness, the numerical results are relatively close to the experimental results, while the theoretical method is a little larger. The relative deviation of the theoretical method is mainly caused by the above assumptions, such as neglecting the nonlinear distribution of stress due to the boundary condition, etc. Noting that the average tensile stiffness predicted by other scholars [41] is 128.33 MN, the theoretical method in this paper can predict a closer result to the true value than the experimental and numerical results. The numerical method includes all the geometric and contact nonlinearities, and can properly predict the axial tensile stiffness, where the relative deviations are mainly caused by the possible initial pre-stress and initial defects in the unbonded flexible riser specimens.

The axial compressive stiffness is also presented in Table 2 with the same boundary condition as the tension case. Since Witz [41] did not present the test results of the compressive case, only analytical and numerical results are calculated and prepared in Table 2, where the numerical results agree well with the analytical results in the case of the riser under axial compression.

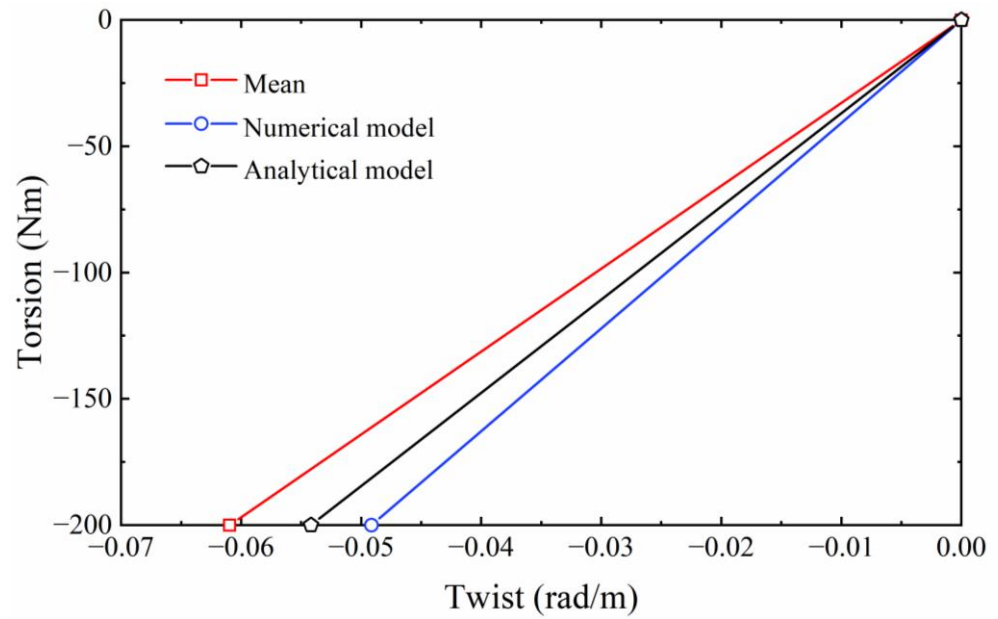
4.2. Clockwise Torsional Behavior of Unbonded Flexible Riser

The clockwise torsional behavior with different boundary conditions is presented in Figure 8. The ratio of kinetic energy to internal energy is also verified to be under 5% during numerical simulation.

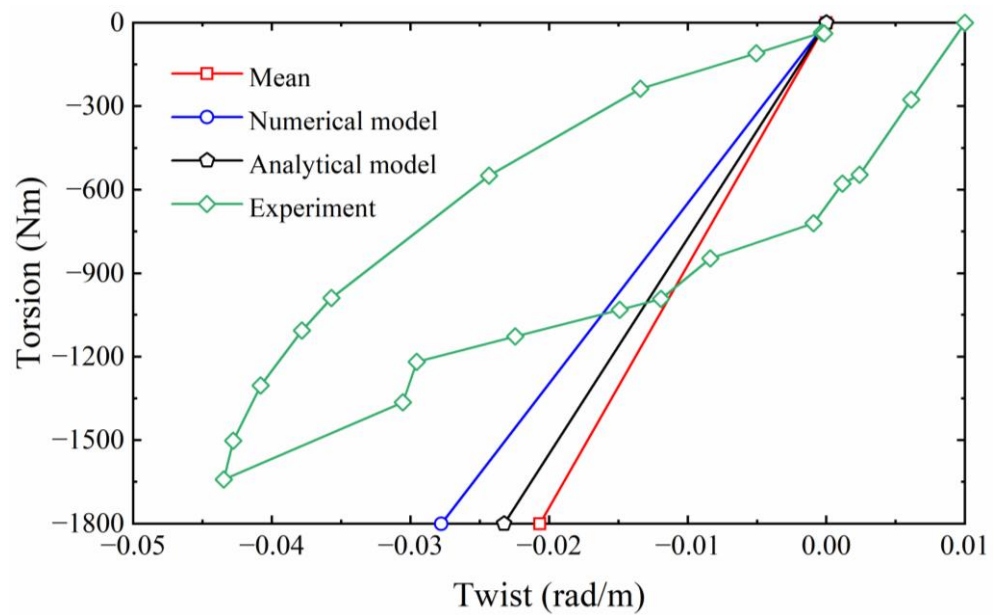
Boundary conditions significantly affect the torsional stiffness. Figure 8 presents the clockwise torsion versus twist curves with different boundary conditions and the corresponding torsional stiffness is presented in Table 3. From Figure 8a, the theoretical and numerical results with the top end free are basically consistent and in good agreement, and the clockwise torsion–twist angle is about linear for both methods. The relative deviation between the theoretical and numerical models is about 2%. The main reason for the error is due to the simplifications and assumptions in the theoretical approach. Additionally, compared with the mean theoretical prediction of clockwise torsional stiffness by organizations and scholars [41], the theoretical method proposed in this paper has a better prediction of the numerical results. From Figure 8b, the theoretical and the numerical results with the top end prevented from moving axially is compared with experimental data. Unlike the numerical and theoretical methods, the test data shows some hysteresis phenomena, and Witz [41] explained that this could be caused by the initial prestressing in the unbonded flexible riser test specimen. The boundary conditions have a great influence on the torsional stiffness, and the torsional stiffness under the restricted axial displacement at the top end is about 20 times more than that with the top end prevented from moving axially.

Table 3. Clockwise torsional stiffness with different models.

Loading Cases	Top End Free (kNm ² /rad)	Top End Prevented from Moving Axially (kNm ² /rad)
Analytical model	4.07	64.80
Numerical model	3.69	77.40
Mean prediction	3.28	87.08



(a)



(b)

Figure 8. Clockwise torsion versus twist curves with different boundary conditions. (a) Clockwise torsion versus twist curves with the top end free. (b) Clockwise torsion versus twist curves with the top end prevented from moving axially.

4.3. Bending Behavior of Unbonded Flexible Riser

A 0.2 MPa initial pressure is applied on the outer sheath first to simulate the pre-stressing by the manufacture of the riser, and then the bending moment is applied on the reference points [12,27]. Figure 9 presents the bending behavior of the unbonded flexible riser by different methods, which both exhibit obvious nonlinear hysteresis phenomena. The full-slipping bending stiffness by different methods is presented in Table 4. Theoretical predictions are in good agreement with both numerical and experimental results. Two loading cases of the theoretical method are presented in this section to be consistent with the numerical and test results. On one hand, the first theoretical prediction did not account for the initial external pressure (consistent with the test setting), and the corresponding

result is a straight line through the origin (the magenta line in Figure 9), where the corresponding bending stiffness is consistent with experimental results. On the other hand, the theoretical prediction has an initial external pressure consistent with the numerical method, and an obvious nonlinear trend is observed in the blue line of Figure 9. The numerical method exhibits obvious nonlinear behavior, which is in good agreement with the test measurement. The curve of numerical method (red line in Figure 9) illustrates three obvious stages when neglecting the instability during numerical simulation. The relative deviation of the full-slipping bending stiffness of the unbonded flexible riser between the analytical and numerical results is relatively small, at only 3.4%.

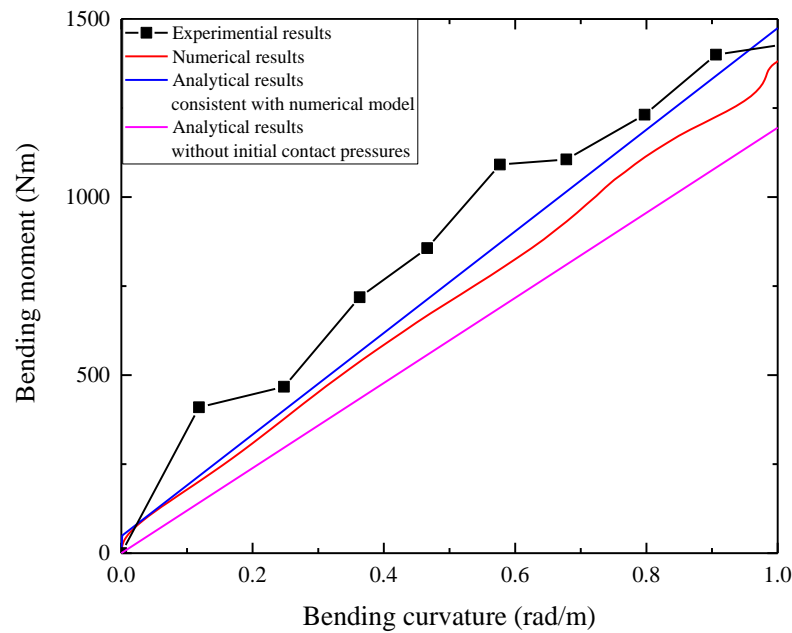


Figure 9. Bending behavior of unbonded flexible riser by different methods.

Table 4. Bending stiffness of full-slipping phase by different methods.

Loading Cases	Without Initial Pressure (kNm ²)	With 02 MPa Initial Pressure (kNm ²)
Analytical method	1.19	1.42
Numerical method	-	1.41
Experimental result	1.190 & 1.041	-

However, the critical bending curvatures when the helical tendon begins to slip for the proposed numerical and analytical methods have some deviation (see Figure 9). The main reason is caused by the contact pressure caused by the bending moment, which the analytical method has ignored. When in the full-slipping phase, the interlayer pressure would no longer have an effect on the bending stiffness, and the corresponding analytical and numerical results are in good agreement.

5. Discussion

An initial external pressure is applied on the outer sheath to simulate the wet environment and the initial prestressing of the riser. Then, the axial tension and compression, the clockwise and counterclockwise torsion, and the bending moment are applied on the reference point. Additionally, the hysteresis behavior under cyclic axial loads is analyzed by outputting the load–displacement curves combined with the friction dissipation energy qualitatively analyzed within the ABAQUS software of 6.13 version.

5.1. Axial Cyclic Behavior of Unbonded Flexible Riser under Cyclic Axial Tension and External Pressure

The corresponding numerical and analytical results are presented in Figure 10. The black line illustrates the numerical results. Due to the initial external pressure, the riser would have an initial axial elongation of about 0.002%. After applying a cyclic axial tension of 6 kN, the numerical curve shows a linear increase, which is mainly due to the effect of the external pressure, which increases the contact pressure between adjacent layers. Thus, the initial gap between adjacent layers is not reduced. Also, the numerical results do not show significant hysteresis characteristics, that is, the first cycle's process and the subsequent cyclic process of the tension–elongation relationship do not present with obvious differences, which is mainly because the extrusion of the layer by a certain external pressure leads to the difficulty of the occurrence of relative displacement of the layer, and friction is still mainly manifested as static friction.

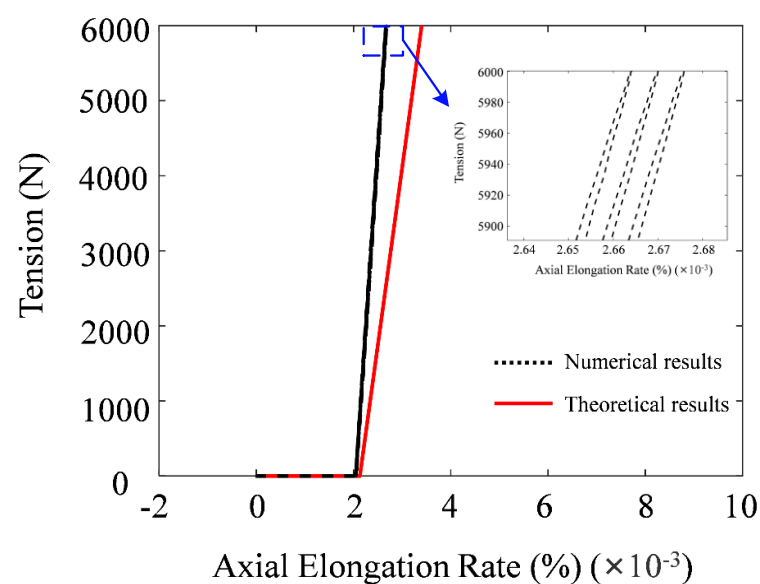


Figure 10. Cyclic axial tensile behavior of unbonded flexible riser under cyclic tension and external pressure.

The red line in Figure 10 represents the theoretical results. The theoretical method integrates the effect of the initial external pressure and axial load. The corresponding axial tension–elongation curve is linear, which is mainly because the theoretical solution process is based on strict assumptions, ignoring the influence of dynamic friction within interlayers and the cross-sectional properties of the carcass and the pressure armor layer.

The numerical results from 5900 to 6000 N are shown in Figure 10. It is found that the unbonded flexible riser still exists within a certain range of hysteresis properties, and its stiffness varies from 225.22 MN to 224.26 MN and the corresponding relative deviation is no more than 0.5%. The reason for the hysteresis is due to the fact that slippage still occurs within the layers during cyclic loading, which leads to an axial force greater than the maximum static friction. This phenomenon is common in such multilayer composite pipes used as marine hoses and cables. Notably, the axial tensile stiffness is increased by 126.39% compared to the case without external pressure (see Table 2) where the interlayers of the unbonded flexible riser are bonded together by the external pressure.

The friction dissipation energy of the system under an external pressure of 1.2 MPa is about 119.5 times that of the system without external pressure during the numerical calculation, which is presented in Table 5. The external pressure makes the interlayer contact pressure greater; under the same friction coefficient, the interlayer friction under 1.2 MPa external pressure is much larger and the axial tension–axial elongation curve under

1.2 MPa external pressure shows a more obvious hysteresis effect than that without external pressure.

Table 5. Frictional energy under cyclic tension during numerical simulation.

Loading Cases	Without Pressure	External Pressure/1.2 MPa
Frictional energy/J	0.308	36.8

5.2. Axial Cyclic Behavior of Unbonded Flexible Riser under Cyclic Axial Compression and External Pressure

Similar to the axial cyclic tension loading condition, the same initial external pressure is applied first, and then the cyclic axial compression of 8 kN is applied on the RP1. The corresponding calculation results by the proposed methods are presented in Figure 11. The external pressure also affects both the axial compressive stiffness and the nonlinear hysteresis behavior, especially for the axial compressive stiffness, which is much greater than the case without external pressure. Furthermore, the hysteresis behavior is also more obvious than the axial tension case, where the axial compressive stiffness has a relative deviation of about 1%.

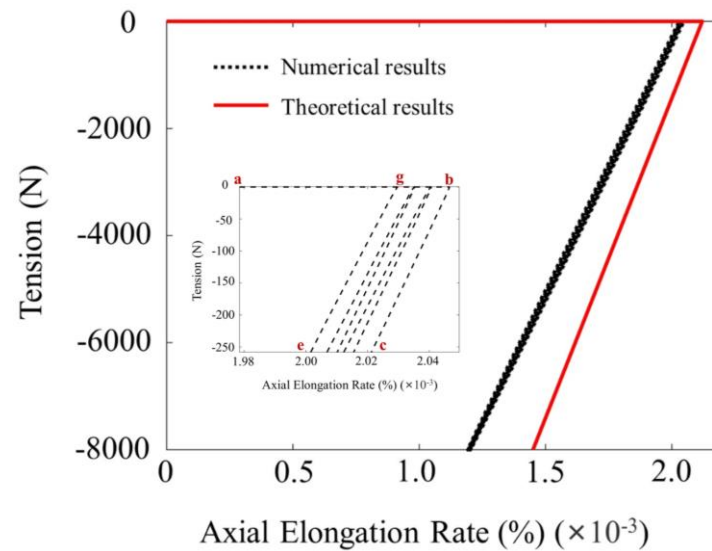


Figure 11. Cyclic axial compressive behavior of unbonded flexible riser under cyclic compression and external pressure.

From Figure 11, the numerical results exhibit a more obvious hysteresis behavior than that under cyclic tension, and the local details of the numerical results from -250 N to 0 N are also presented in Figure 11: (1) stage a to b is the axial deformation caused by the initial external pressure, which is consistent with the tension loading case; (2) then, after applying the axial compression, the axial elongation of the riser increases with the increasing compression; (3) with the unloading of the axial compression, the compressive behavior of the unbonded flexible riser shows some nonlinearity, and finally returns to point g in Figure 8, which is far away from the initial point b. In addition, the corresponding axial compressive stiffness of the unbonded flexible riser ranges from 94.34 MN to 95.58 MN during the numerical simulation, which is much greater than that without external pressure in Table 2. As a comparison, the axial compressive stiffness calculated by the theoretical method is 110.94 MN, and the relative deviation is about 15%. Both theoretical and numerical results show a greater increase of the axial compressive stiffness, which is mainly due to the fact that when loading the external pressure, the interlayers are in closer contact and the gap between adjacent layers is reduced, contributing to the

increasing friction that leads to a substantial increase in the axial compressive stiffness of the unbonded flexible riser.

5.3. Behavior of Unbonded Flexible Riser under Cyclic Torsion and External Pressure

For the hysteresis response of the unbonded flexible riser under cyclic torque loading, the torque is taken as 40 NM. The effect of external pressure, which is taken as 0.6 MPa, 1.2 MPa, and 1.8 MPa, is also considered and applied on the outer sheath. Also, a quasi-static loading is applied in this paper.

Figure 12 describes the torsion–twist angle curve of different loading conditions. As the theoretical model ignores the influence of frictional contact in the calculation process, the torsion–twist angle curve cannot accurately reflect the hysteresis characteristics, and the torsional stiffness of the theoretically calculated unbonded flexible risers is consistent under three external pressures. In order to make the graph more concise and clearer, Figure 12 only shows the theoretical results under the external pressure of 0.6 MPa. From Figure 12, the horizontal line indicates the initial amount of torsion of the riser after applying the external pressure only. The following conclusions can be drawn from the analysis of the calculation results:

1. The difference between theoretical and numerical results is small. Taking 0.6 MPa as an example, the torsional stiffness obtained by theoretical calculation is 173.52 N·m²/rad, and the torsional stiffness obtained by numerical calculation is 160.02 N·m²/rad. The relative error is about 8.4%, which is mainly because the theoretical calculation process is based on a relatively strict assumption for the solution, ignoring the influence of mutual contact between the helical tendon.
2. Under the same external pressure condition, the torsional stiffness of loading clockwise torque is almost the same as that of loading counterclockwise torque. This is different from the torsional stiffness when loaded without external pressure, where counterclockwise torque stiffness is about 40 times higher than that of clockwise torque stiffness [44]. The reason is that when no external pressure is applied, due to the counterclockwise helical structure of the tensile armor layer, loading the counterclockwise torque makes the external tensile armor layer tighten along the circle direction, the layers do not separate, and the riser as a whole exhibits higher torsional capacity. While loading the clockwise torque, the external tensile armor layer helical steel tendon expands along the circle direction, the interlayers separate, and the riser exhibits lower torsional stiffness. When under external pressure, each layer is compressed, and the interlayers do not separate, which shows higher torsional stiffness.
3. With the increasing of external pressure, the unbonded riser shows more obvious hysteresis characteristics, i.e., the curves do not completely overlap in the cyclic process, which is mainly due to the exertion of a certain amount of pressure on the interlayer resulting in the interlayer not being easily relatively displaced. Furthermore, the friction between the interlayer is gradually increased, so that the torsion–twist angle curves show a more pronounced hysteresis response.

Table 6 shows the numerically calculated frictional dissipation energy under three different external pressure loading conditions. With the increasing of external pressure, the frictional dissipation energy increases gradually, which further proves that the interlayer frictional slip generated by the loading of unbonded flexible risers with external pressure is one of the main reasons for the hysteresis phenomenon.

Table 6. Frictional energy under cyclic torsion during numerical simulation.

Loading Cases	0.6 MPa	1.2 MPa	1.8 MPa
Frictional energy /J	9.94	52.39	123.28

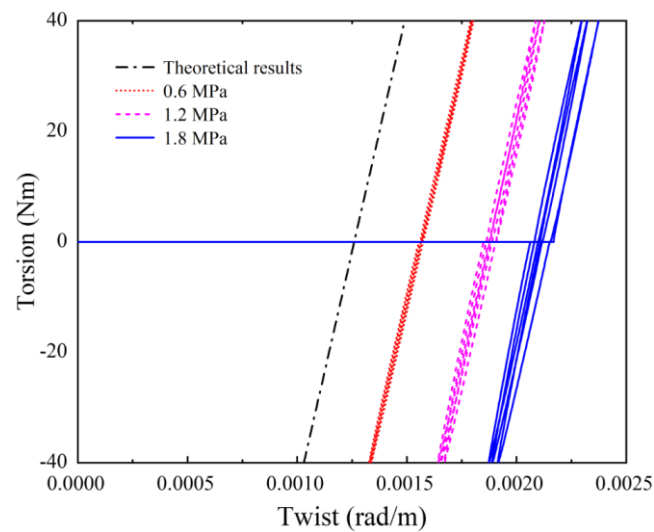


Figure 12. Axial cyclic torsion–twist curves of different cases.

5.4. Bending Behavior of Unbonded Flexible Riser under Bending Moment and Irregular External and Internal Pressure

When unbonded flexible risers are in the actual working environment, due to the actual configuration, the internal and external pressure loads acting on the inner and outer sheath layers might not be uniformly distributed along the length of the riser, but rather show a linear variation with the depth at which the unbonded flexible riser is located.

Considering the loading cases of applying external and internal pressure respectively, six calculation conditions are given by the numerical method as shown in Table 7, and the friction coefficients are all taken as 0.1. Among them, loading cases A1 and B1 are the control cases, assuming that the non-uniform pressure acting on the inner and outer sheath layers of unbonded flexible risers can be equated to the corresponding uniformly distributed pressure effects, and the uniformly distributed internal and external pressure effects of 0.5 MPa are taken as the reference conditions. Loading cases A2 and B2 apply significantly varying external and internal pressures to the external and internal sheath layers of the unbonded flexible riser, respectively, and the corresponding pressures vary linearly along the length of the unbonded flexible riser from 0 MPa to 1 MPa. For cases A3 and B3, the unbonded flexible riser model is considered to be at a certain water depth and the riser model is perpendicular to the seabed direction, and it is assumed that the pressure action acting on the corresponding inner and outer sheath layers varies linearly along the direction of the water depth (linearly in the range of 0 MPa to 0.01 MPa); an initial pressure of 0.495 MPa is applied to the corresponding layer structure, considering that it is comparable to the action of the internal and external pressure loads acting in cases A2 and B2.

The pressure contours for the external sheath layer, the external tensile armor layer, and the internal tensile armor layer are given for cases A1 and A2, respectively, as shown in Figure 13. Compared with Figure 13b, it can be seen that the outer sheath layer with non-uniformly distributed external pressure exhibits obvious pressure nonlinearity when neglecting the influence of boundary effects. The pressure contours of the external tensile armor layer structure adjacent to the outer sheath layer are shown in Figure 13c,d, and there is little difference between the two types of pressure. A similar phenomenon can be observed for the internal tensile armor layer structure (Figure 13e,f).

Table 7. Geometric and material properties of unbonded flexible riser model.

Pressure	Case Number	Distribution of Pressure	Range of Pressure/MPa	Initial Pressure/MPa
External pressure	A1	Uniform distribution	-	0.5
	A2	Non-uniform distribution	From 0 to 1	-
	A3	Non-uniform distribution	From 0 to 0.01	0.495
Internal pressure	B1	Uniform distribution	-	0.5
	B2	Non-uniform distribution	From 0 to 1	-
	B3	Non-uniform distribution	From 0 to 0.01	0.495

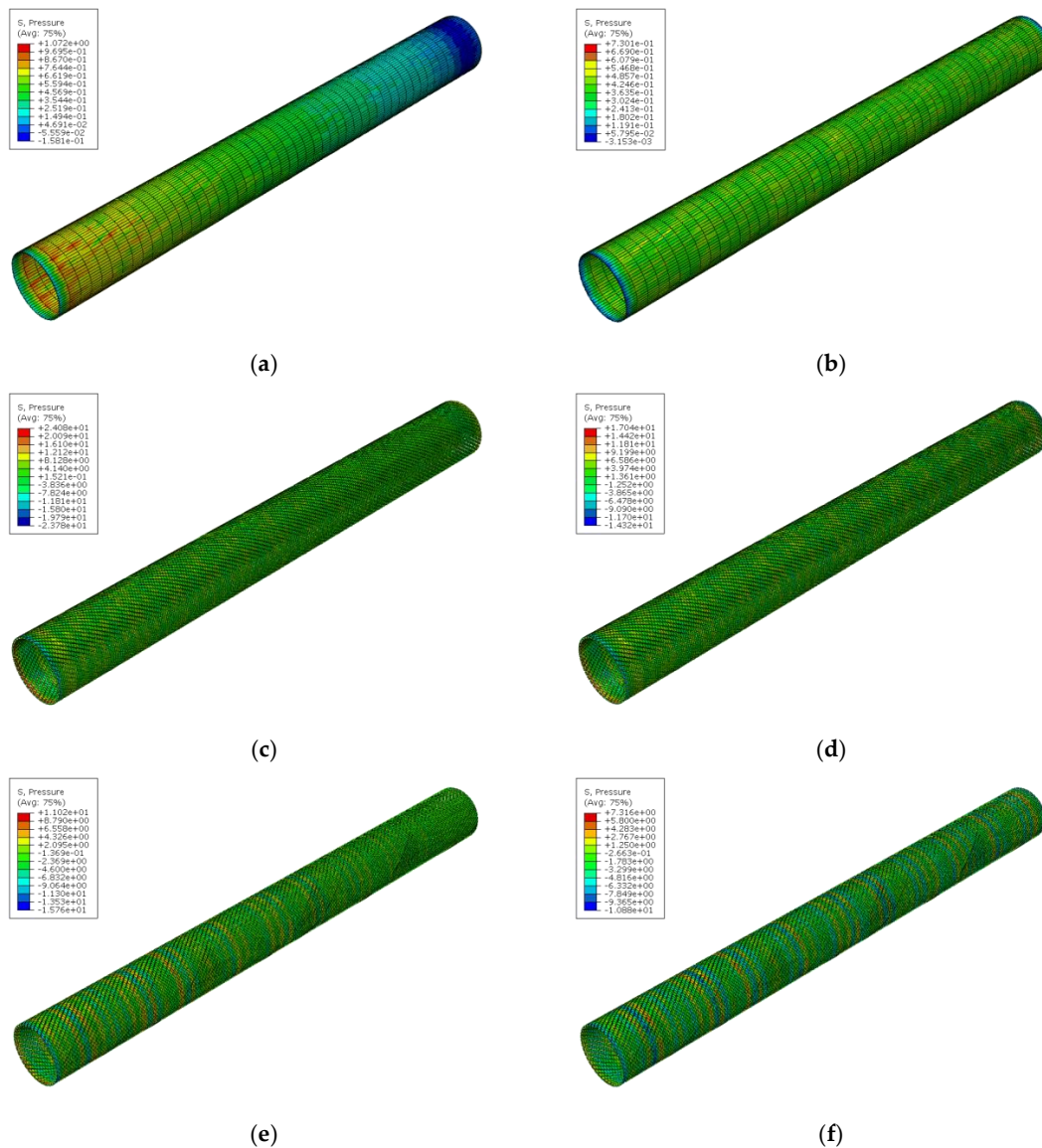


Figure 13. Pressure contours of the numerical riser model under a wide range of non-uniform external pressures and equivalent uniform external pressures. (a) Outer sheath, non-uniform external pressure from 0 to 1 MPa. (b) Outer sheath, uniform external pressure of 0.5 MPa. (c) Outer tensile armor layer, non-uniform external pressure from 0 to 1 MPa. (d) Outer tensile armor layer, uniform external pressure of 0.5 MPa. (e) Inner tensile armor layer, non-uniform external pressure from 0 to 1 MPa. (f) Inner tensile armor layer, uniform external pressure of 0.5 MPa.

The bending moment–curvature curves for the three cases are given in Figure 14, where the black solid line is the theoretical prediction, the violet solid curve represents A1, and the dashed curves represent A2 and A3. In the full slip stage, the theoretical method has better predictions and the full slip bending stiffnesses obtained by the two methods are close to each other. Neglecting the instability of the numerical model, it can be seen from Figure 14 that the mechanical properties under combinations of different forms of external pressure and bending moment maintain a good agreement. In particular, in the case where the range of variation of the external pressure distributed along the pipe length direction is not significant (Case A3), the numerical results are in good agreement with the results of the numerical calculation of the equivalent uniformly loaded external pressure (Case A1). Therefore, for the numerical modeling of unbonded flexible risers of limited length, the external non-uniform pressure distribution acting on the risers can be equated to a uniformly distributed external pressure load with the same value of total pressure in the study of their bending characteristics.

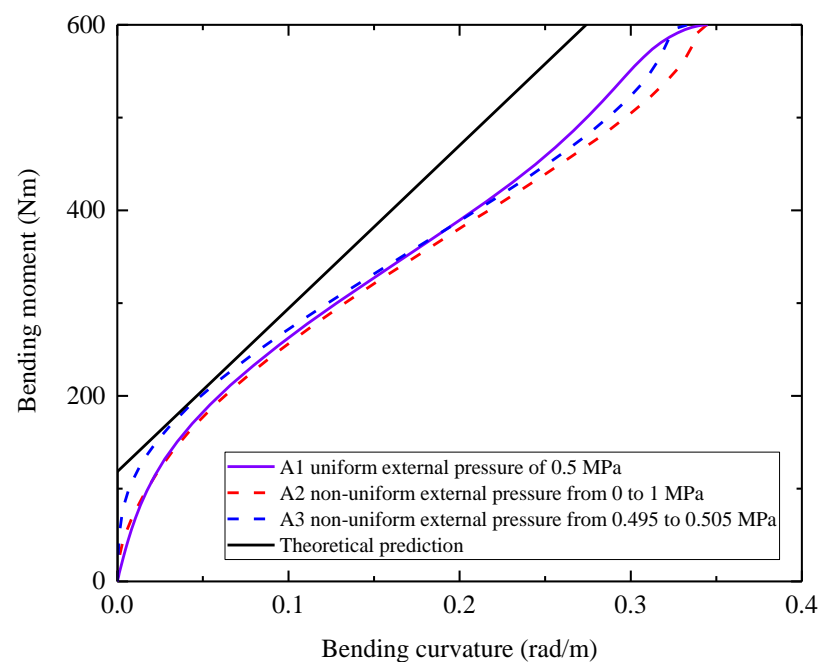


Figure 14. Bending behavior under non-uniform external pressure and equivalent uniform external pressure.

Since the innermost carcass layer is a non-watertight layer structure, the internal pressure acts on the internal sheath layer of the unbonded flexible riser. Considering the different loading forms of internal pressure loads, the pressure contours of the numerical model of the unbonded flexible riser after the application of internal pressure are given in Figure 15. Comparison of the pressure contours of different layers for the case B2, which has a large variation of the internal pressure load along the pipe length direction, and the control case B1, which has a uniformly loaded internal pressure load, are given. Neglecting the influence of the boundary condition, consistent with the non-uniformly loaded external pressure loading case, the non-uniform distribution of internal compressive load is obvious in the inner sheath layer, as shown in Figure 15a, whereas the corresponding uniformly loaded internal pressure of the control case (as shown in Figure 15b) has a uniform distribution after loading. The pressure distribution level of the corresponding internal and external tensile armor layers is comparable (Figure 15c–f). Unlike the cases A1 to A3, due to the detailed simulation of the pressure armor layer, the effect of the internal pressure on the external and internal tensile armor layers is limited, especially for the external tensile armor structure, which suffers from a very low pressure level (Figure 15e,f).

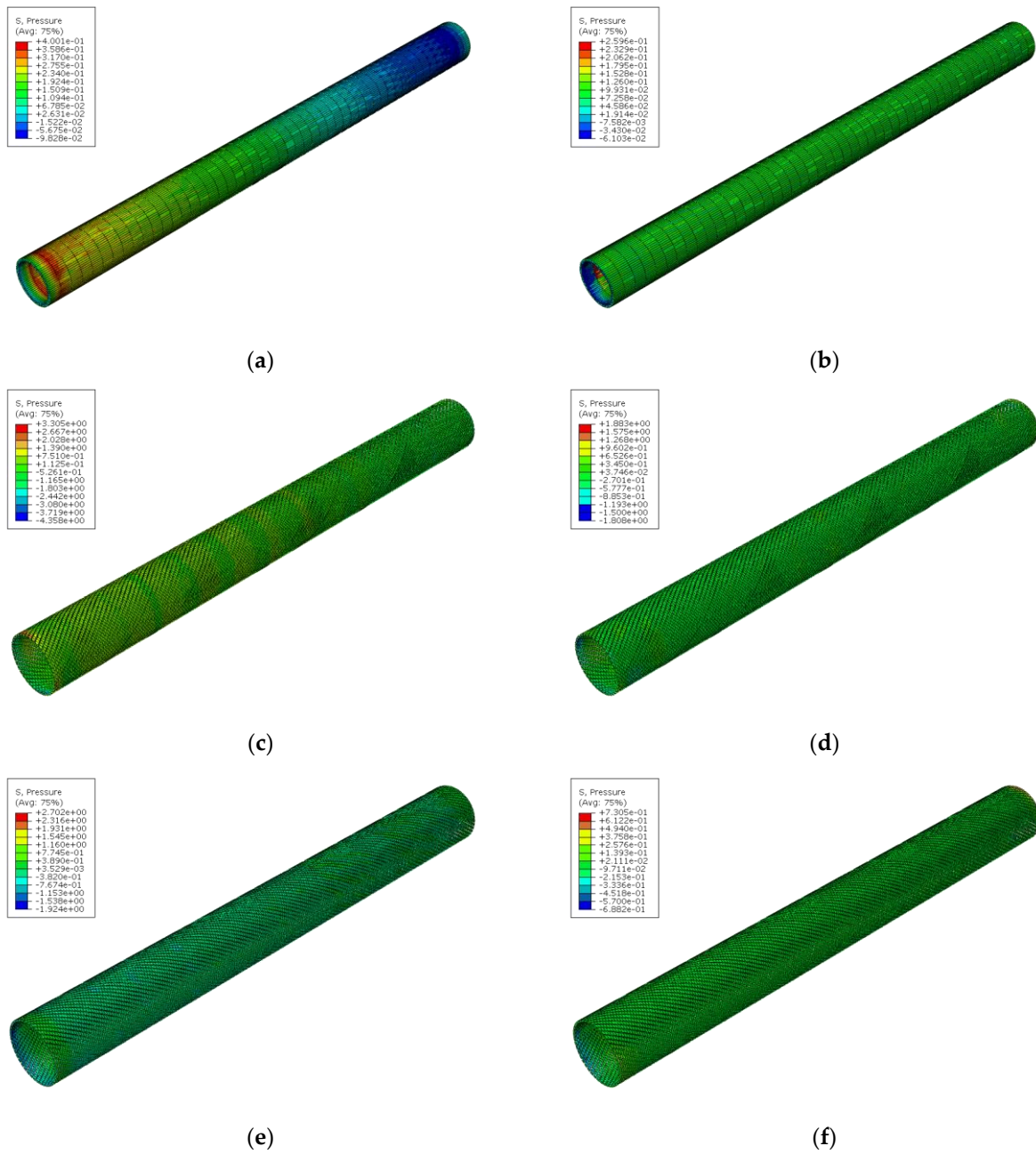


Figure 15. Pressure contours of the numerical riser model under a wide range of non-uniform internal pressures and equivalent uniform internal pressures. (a) Inner sheath, non-uniform internal pressure from 0 to 1 MPa. (b) Inner sheath, uniform internal pressure of 0.5 MPa. (c) Inner tensile armor layer, non-uniform internal pressure from 0 to 1 MPa. (d) Inner tensile armor layer, uniform internal pressure of 0.5 MPa. (e) Outer tensile armor layer, non-uniform internal pressure from 0 to 1 MPa. (f) Outer tensile armor layer, uniform internal pressure of 0.5 MPa.

The bending behavior of the unbonded flexible riser for loading cases from B1 to B3 are given in Figure 16. The numerical results show good agreement in general, and the different internal pressure loading methods have limited influence on the numerical results. The corresponding theoretical prediction is presented as the black solid line in Figure 16. There is a certain difference between the theoretical and numerical results, which is due to the fact that the numerical model in this paper adequately takes into account the actual geometry of the pressure armor layer (Zeta layer). The pressure armor layer is the most important internal pressure-bearing layer of the unbonded flexible riser. It is positioned

next to the inner sheath layer and it resists the radial loads due to its special geometry. After applying the internal pressure, the pressure armor layer carries most of the internal pressure and only a small portion of the internal pressure is transferred to the outer layers, e.g., internal and external tensile armor layers.

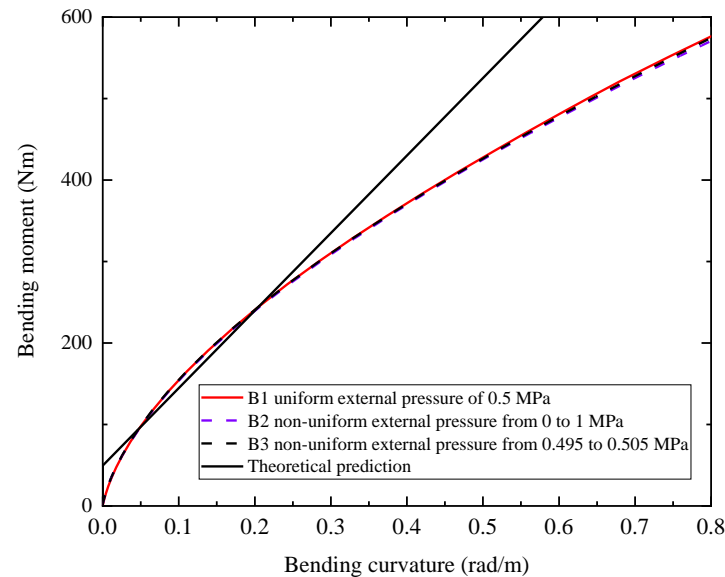


Figure 16. Bending behavior under non-uniform internal pressure and equivalent uniform internal pressure.

6. Conclusions

This paper presents the nonlinear behavior of unbonded flexible risers under irregular loads. Firstly, the theoretical model is derived by function principles. Then, based on a typical 2.5-inch unbonded flexible riser model with eight layers, the numerical model is established by a combination of separate interlayers with detailed geometric properties. After the verification through Witz's experimental case, the proposed numerical and theoretical methods can possibly predict the nonlinear behavior and are in good agreement. Some useful conclusions are drawn in this section:

1. The axial stiffness of the unbonded flexible riser under cyclic axial force would show a certain hysteresis characteristic, and the corresponding axial stiffness would change in a certain small range, while the overall behavior is still close to a linear change. The external pressure would enhance the axial stiffness of unbonded flexible riser and the axial compressive behavior is especially sensitive to the external pressure, not only in the form of a significant increase in compressive stiffness, but also in the form of a more obvious hysteresis phenomenon.
2. When under cyclic torsion and external pressure, the friction under the external pressure can lead to hysteresis characteristics. As the external pressure increases, the interlayer friction increases, the slip decreases, and the frictional dissipation energy increases significantly, affecting the torsional stiffness significantly.
3. The bending characteristics of an unbonded flexible riser under irregular distributed internal and external pressures that vary linearly along its own length can be equated to the bending characteristics under equivalent uniformly distributed internal and external pressures. The linearly distributed internal and external pressure effects are only more pronounced in the corresponding layer structure where the internal and external pressure loads are applied, and the internal layer (especially the tensile armor layer) is subjected to comparable levels of pressure.

In conclusion, the proposed method's ability to capture the intricate dynamics of tensile armor layer slippage under various load conditions has profound implications

for the design, deployment, and maintenance of deep-sea oil and gas infrastructure. By enhancing predictive capabilities, the corresponding work can contribute to a reduction in the risk of structural failure, which is paramount for the safety and economic viability of offshore operations. The findings, particularly the insights into the hysteresis phenomenon and the effects of external pressure on axial and torsional stiffness, provide a foundation for further research and development in the field. The model can be utilized to optimize riser design, improve the reliability of load predictions, and inform maintenance schedules to prevent costly downtime.

Author Contributions: Conceptualization, Q.L. and Z.Q.; methodology, Q.L.; software, Z.Q. and X.L.; validation, J.H.; formal analysis, G.W.; investigation, S.W. and F.C.; resources, Q.L., S.W. and F.C.; data curation, Z.Q.; writing—original draft preparation, Q.L. and Z.Q.; writing—review and editing, S.W.; visualization, X.L.; supervision, F.C.; project administration, G.W.; funding acquisition, Q.L., S.W. and F.C. All authors have read and agreed to the published version of the manuscript.

Funding: This paper was funded by the National Natural Science Foundation of China (Grant No. 52102425 & 52205027), the Natural Science Foundation of Jiangsu Province (Grant No. BK20220500 & BK20220496), and the Jiangsu Funding Program for Excellent Postdoctoral Talent (Grant No. 2022ZB560).

Institutional Review Board Statement: Not applicable.

Informed Consent Statement: Not applicable.

Data Availability Statement: Data are contained within the article.

Conflicts of Interest: The authors declare no conflicts of interest.

References

- Goto, Y.; Okamoto, T.; Araki, M.; Fuku, T. Analytical study of the mechanical strength of flexible pipes. *Brain Dev.* **1987**, *109*, 249–253. [[CrossRef](#)]
- Mcnamara, J.F.; Harte, A.M. Three-Dimensional analytical simulation of flexible pipe wall structure. *J. Offshore Mech. Arct. Eng.* **1992**, *114*, 69–75. [[CrossRef](#)]
- Harte, A.M.; Mcnamara, J.F. Modeling procedures for the stress analysis of flexible pipe cross sections. *J. Offshore Mech. Arct. Eng.* **1993**, *115*, 46–51. [[CrossRef](#)]
- Witz, J.A.; Tan, Z. On the axial-torsional structural behaviour of flexible pipes, umbilicals and marine cables. *Mar. Struct.* **1992**, *5*, 205–227. [[CrossRef](#)]
- Claydon, P.; Cook, G.; Brown, P.A.; Chandwani, R. A theoretical approach to prediction of service life of unbonded flexible pipes under dynamic loading conditions. *Mar. Struct.* **1992**, *5*, 399–429. [[CrossRef](#)]
- Lanteigne, J. Theoretical estimation of the response of helically armored cables to tension, torsion, and bending. *J. Appl. Mech.* **1985**, *52*, 423–432. [[CrossRef](#)]
- Mciver, D.B. A method of modeling the detailed component and overall structural behavior of flexible pipe sections. *Eng. Struct.* **1995**, *17*, 254–266. [[CrossRef](#)]
- Ramos, R., Jr.; Pesce, C.P.; Martins, C.A. A new analytical expression to estimate the bending stiffness of flexible risers. In Proceedings of the International Conference on Offshore Mechanics and Arctic Engineering, Cancun, Mexico, 8–13 June 2003; OMAE2003-37320.
- Wang, K.; Ji, C. Helical wire stress analysis of unbonded flexible riser under irregular response. *J. Mar. Sci. Appl.* **2017**, *16*, 208–215. [[CrossRef](#)]
- Wang, K.; Ji, C.; Xue, H.; Tang, W. Fatigue damage study of helical wires in catenary unbonded flexible riser near touchdown point. *J. Offshore Mech. Arct. Eng.* **2017**, *139*, 051701. [[CrossRef](#)]
- Féret, J.J.; Bournazel, C.L. Calculation of stresses and slip in structural layers of unbonded flexible pipes. *J. Offshore Mech. Arct. Eng.* **1987**, *109*, 263–269. [[CrossRef](#)]
- Kebadze, E. Theoretical Modelling of Unbonded Flexible Pipe Cross-Sections. Ph.D. Thesis, South Bank University, London, UK, 2000.
- Kraincani, I.; Kebadze, E. Slip initiation and progression in helical armouring layers of unbonded flexible pipes and its effect on pipe bending behaviour. *J. Strain Anal. Eng. Des.* **2001**, *36*, 265–275. [[CrossRef](#)]
- Dong, L.; Huang, Y.; Zhang, Q.; Liu, G. An analytical model to predict the bending behavior of unbonded flexible pipes. *J. Ship Res.* **2013**, *57*, 171–177. [[CrossRef](#)]

15. Karathanasopoulos, N.; Ganghoffer, J.F.; Papailiou, K.O. Analytical closed-form expressions for the structural response of helical constructions to thermal loads. *Int. J. Mech. Sci.* **2016**, *117*, 258–264. [[CrossRef](#)]
16. Hong, K.J.; Kiureghian, A.D.; Sackman, J.L. Bending Behavior of Helically Wrapped Cables. *J. Eng. Mech.* **2005**, *131*, 500–511. [[CrossRef](#)]
17. Dai, T.; Sævik, S.; Ye, N. An anisotropic friction model in non-bonded flexible risers. *Mar. Struct.* **2018**, *59*, 423–443. [[CrossRef](#)]
18. Dai, T.; Sævik, S.; Ye, N. Friction models for evaluating dynamic stresses in non-bonded flexible risers. *Mar. Struct.* **2017**, *55*, 137–161. [[CrossRef](#)]
19. Dong, L.; Qu, Z.; Zhang, Q.; Huang, Y.; Liu, G. A general model to predict torsion and curvature increments of tensile armors in unbonded flexible pipes. *Mar. Struct.* **2019**, *67*, 102632. [[CrossRef](#)]
20. Yun, R.H.; Jang, B.S.; Kim, J.D. Improvement of the bending behavior of a flexible riser: Part I—Nonlinear bending behavior considering the shear deformation of polymer layers. *Appl. Ocean Res.* **2020**, *101*, 102204. [[CrossRef](#)]
21. Sousa, J.R.J.; Pinho, A.N.; Ellwanger, G.B.; Lima, E.C.P. Numerical analysis of a flexible pipe with damaged tensile armor wires. In Proceedings of the International Conference on Ocean, Offshore and Arctic Engineering, Honolulu, HI, USA, 31 May–5 June 2009; OMAE2009-80014.
22. Cruz, F.T.F. Structural Analysis of Flexible Pipes through the Finite Element Method. Master's Thesis, EPUSP, Sao Paulo, Brazil, 1996.
23. Bahtui, A.; Bahai, H.; Alfano, G. A finite element analysis for unbonded flexible risers under axial tension. In Proceedings of the International Conference on Offshore Mechanics and Arctic Engineering, Estoril, Portugal, 15–20 June 2008. OMAE2008-57627.
24. Bahtui, A.; Bahai, H.; Alfano, G. A finite element analysis for unbonded flexible risers under torsion. *J. Offshore Mech. Arct. Eng.* **2008**, *130*, 041301. [[CrossRef](#)]
25. Perdrizet, T.; Leroy, J.-M.; Barbin, N.; Le-Corre, V.; Charliac, D.; Estrier, P. Stresses in armour layers of flexible pipes: Comparison of Abaqus models. In Proceedings of the SIMULIA Customer Conference, Barcelona, Spain, 17–19 May 2011; pp. 1–14.
26. Leroy, J.-M.; Perdrizet, T.; Le Corre, V.; Estrier, P. Stress assessment in armour layers of flexible risers. In Proceedings of the International Conference on Ocean, Offshore and Arctic Engineering, Shanghai, China, 6–11 June 2010; OMAE2010-20932.
27. Zhang, M.; Chen, X.; Fu, S.; Guo, Y.; Ma, L. Theoretical and numerical analysis of bending behavior of unbonded flexible risers. *Mar. Struct.* **2015**, *44*, 311–325. [[CrossRef](#)]
28. Zhang, H.; Tong, L.; Addo, M.A.; Liang, J.; Wang, L. Research on contact algorithm of unbonded flexible riser under axisymmetric load. *Int. J. Press. Vessel. Pip.* **2020**, *188*, 104248. [[CrossRef](#)]
29. Lu, H.; Vaz, M.A.; Caire, M. Alternative analytical and finite element models for unbonded flexible pipes under axisymmetric loads. *Ocean Eng.* **2021**, *225*, 108766. [[CrossRef](#)]
30. Tang, L.; He, W.; Zhu, X.; Zhou, Y. Mechanical analysis of unbonded flexible pipe tensile armor under combined loads. *Int. J. Press. Vessel. Pip.* **2019**, *171*, 217–223. [[CrossRef](#)]
31. Ebrahimi, A.; Kenny, S.; Hussein, A. Finite element investigation on the tensile armor wire response of flexible pipe for axisymmetric loading conditions using an implicit solver. *J. Offshore Mech. Arct. Eng.* **2018**, *140*, 041402. [[CrossRef](#)]
32. Li, J.Y.; Qiu, Z.X.; Ju, J.S. Numerical modeling and mechanical analysis of flexible risers. *Math. Probl. Eng.* **2014**, *2015*, 894161. [[CrossRef](#)]
33. Liu, M.; Li, J.Y.; Chen, L.; Ju, J. On the response and prediction of multi-layered flexible riser under combined load conditions. *Eng. Comput.* **2019**, *36*, 2507–2529. [[CrossRef](#)]
34. Yoo, D.H.; Jang, B.S.; Yim, K.H. Nonlinear finite element analysis of failure modes and ultimate strength of flexible pipes. *Mar. Struct.* **2017**, *54*, 50–72. [[CrossRef](#)]
35. Ren, S.; Tang, W.Y.; Guo, J.T. Behavior of unbonded flexible risers subject to axial tension. *China Ocean Eng.* **2014**, *28*, 249–258. [[CrossRef](#)]
36. Ren, S.; Xue, H.; Tang, W. Analytical and numerical models to predict the behavior of unbonded flexible risers under torsion. *China Ocean Eng.* **2016**, *30*, 243–256. [[CrossRef](#)]
37. Ren, S.; Tang, W.; Kang, Z.; Geng, H. Numerical study on the axial-torsional response of an unbonded flexible riser with damaged tensile armor wires. *Appl. Ocean Res.* **2020**, *97*, 102045. [[CrossRef](#)]
38. Liu, Q.; Xue, H.; Tang, W.; Yuan, Y. Theoretical and numerical methods to predict the behavior of unbonded flexible riser with composite armor layers subjected to axial tension. *Ocean Eng.* **2020**, *199*, 107038. [[CrossRef](#)]
39. Liu, Q.; Xue, H.; Tang, W. Behavior of unbonded flexible riser with composite armor layers under coupling loads. *Ocean Eng.* **2021**, *239*, 109907. [[CrossRef](#)]
40. Ramos, R., Jr.; Kawano, A. Local structural analysis of flexible pipes subjected to traction, torsion and pressure loads. *Mar. Struct.* **2015**, *42*, 95–114. [[CrossRef](#)]
41. Witz, J.A. A case study in the cross-section analysis of flexible risers. *Mar. Struct.* **1996**, *9*, 885–904. [[CrossRef](#)]
42. Bahtui, A. Development of a Constitutive Model to Simulate Unbonded Flexible Riser Pipe Elements. Ph.D. Thesis, Department of Mechanical Engineering Brunel University, London, UK, 2008.

43. Sævik, S.; Berge, S. Fatigue testing and theoretical studies of two 4 in flexible pipes. *Eng. Struct.* **1995**, *17*, 276–292. [[CrossRef](#)]
44. Ren, S. Study on Cross-Sectional Mechanical Properties and Typical Failure Characteristics of Unbonded Flexible Risers. Ph.D. Thesis, Shanghai Jiaotong University, Shanghai, China, 2016.

Disclaimer/Publisher’s Note: The statements, opinions and data contained in all publications are solely those of the individual author(s) and contributor(s) and not of MDPI and/or the editor(s). MDPI and/or the editor(s) disclaim responsibility for any injury to people or property resulting from any ideas, methods, instructions or products referred to in the content.